J Mater Sci (2010) 45:5649–5659
DOI 10.1007/s10853-010-4630-1

Quantitative evaluation of high temperature deformation mechanisms: a specific microgrid extensometry technique coupled with EBSD analysis

A. Soula · D. Locq · D. Boivin · Y. Renollet · P. Caron · Y. Bréchet

Received: 23 February 2010 / Accepted: 17 May 2010 / Published online: 8 June 2010

Abstract A microgrid extensometry method has been developed and used to obtain information about intragranular and intergranular creep mechanisms. An oxide grid was deposited on a creep specimen using an electron lithography technique. This oxide grid offers high backscattered electron contrast and can withstand long duration creep tests under vacuum in the 700–850 °C range without degradation. Specific methods were used to measure in-plane displacements at the grid nodes or at the grain boundaries using correlation of grid images taken before and after the creep test. The local strain and grain boundary sliding (GBS) data were then calculated. Combined information about grain boundary crystallography and GBS has been obtained by superimposing the electron backscattered diffraction (EBSD) map on the deformation maps. To illustrate the potential of this set of processes, two examples of application on a nickel-base disc superalloy are presented. The first one concerns the influence of the creep temperature on the local strain and the GBS. The second application quantitatively shows the influence of grain boundary character on GBS of this material.

A. Soula · D. Locq (✉) · D. Boivin · Y. Renollet · P. Caron
Département des Matériaux et Structures Métalliques, Office National d'Études et de Recherches Aérospatiales (ONERA), BP 72, 92322 Châtillon Cedex, France
e-mail: didier.locq@onera.fr

Y. Bréchet
SIMaP, BP 75, 38402 St Martin d'Hères Cedex, France

Present Address:
A. Soula
Michelin, site de Ladoux, 63040 Clermont-Ferrand Cedex 9, France

Introduction

The development of creep resistant alloys is becoming more and more a key engineering issue, for propulsion engine in aeronautics as well as for thermal or nuclear energy production. There is an abundant literature on creep mechanisms, either intragranular (diffusional creep or dislocation mediated creep), or, to a lesser extent, intergranular (grain boundary sliding), and the Ashby deformation maps provide a guideline to estimate the relative importance of the various mechanisms for steady state conditions [1]. However, the detailed and quantitative experimental information on the effect of temperature, applied stress and global strain on the occurrence of grain boundary sliding (GBS), for industrial alloys, is sparse. In the perspective of possible grain boundary engineering, it is also of relevance to obtain information on the influence of grain boundary (GB) crystallographic character. Getting this information requires a tool providing local data on the magnitude of intragranular deformation and GBS, at the same time as local data about crystallographic nature of grains boundaries and crystallographic orientation of grains.

Grids or microgrids, developed in the 1970s to replace the scratch technique [2–4], are widely used for GBS analysis. The grid technique presents the advantage of a two-direction measurement in the plane of the sample surface, over the unidirectional one provided by the scratch technique. Gold or platinum microgrids are generally used for micromechanical investigations at room or intermediate temperatures (up to 500 °C) [4–6]. However, at higher temperatures, thermal and environmental degradations are rapidly becoming a serious issue. As an alternative, internal microgrids engraved by etching were used to study the deformation of a duplex stainless steel at 1050 °C in air

[7]. A microextensometry technique, using a microgrid made of hafnia has been specifically developed for analysis of GBS during creep at high temperature (700–800 °C) of a nickel-base superalloy for turbine disc applications [8, 9]. This technique was shown to be very efficient to reveal local deformation and allowed to confirm that GBS contributes to the high temperature creep deformation of such alloys [8]. Coupled with electron backscatterered diffraction (EBSD), this microextensometry technique reveals that GBS mainly concerns the general grain boundaries favourably oriented at about 45° of the tensile stress axis [9].

The aim of the present paper is to provide a comprehensive description of this microgrid extensometry technique, including details about the grid material selection and the deposition method. The specific requirements associated with high temperature testing set some special difficulties which are worth explaining in detail in order to give the present method its full applicability. The method of coupling with EBSD analysis is described and two examples of applications illustrate the potential of this extensometry technique for studying the high temperature creep behaviour of the NR6 disc superalloy.

Experimental method

Selection of the grid material

Microgrids used to measure the displacement field at the surface of specimens tested in creep must satisfy to several requirements mainly because of the long durations and the high temperatures characteristic of this type of mechanical test:

1. high contrast in backscattered electron detection between the specimen material and the grid materials,
2. thermal and environmental stability of the microgrid, for the duration of the creep test,
3. high temperature mechanical properties, and in particular a sufficient ductility.

The method to evaluate the deformation is based on digital image correlation of a given grid pattern before and after deformation. The first criterion is to obtain scanning electron microscopy (SEM) images with a sufficient contrast between the grid and the substrate (in the present example, a nickel-base superalloy). The high quality SEM images are achieved using backscattered electron (BSE) emission. This SEM mode is used to detect chemical contrast, so the backscatter factor (η_r) of the grid material should be significantly different from the superalloy's one. This chemical contrast must remain significant after the creep test. To ensure this, the creep experiments are conducted under high vacuum ($\sim 10^{-4}$ Pa) to avoid excessive oxidation of the superalloy and of the grid material. Meanwhile, the grid material must exhibit an excellent resistance to thermal and environmental damage. And finally, it should exhibit a good high temperature deformability to reveal the superalloy deformation without undesirable cracking or detachment of the grid.

Table 1 Physical properties of the tested grid materials

Material	Melting point (°C)	Backscattering factor (η_r) [10]	Results after 750 °C exposure
Au	1064	0.487	Contrast loss
Au/Pd (60/40) wt%	~1470	0.451	Contrast loss
Pt	1772	0.485	Dispersion
Cr	1857	0.263	Low contrast and contrast loss
$MoSi_2$	~2020	0.300	Pest oxidation
WSi_2	~2160	0.403	Pest oxidation
Mo	2617	0.380	Oxidation
ZrO_2	~2700	0.298	Ok
HfO_2	~2774	0.414	Ok and higher contrast
W	3410	0.476	Oxidation

Several refractory materials were selected to be tested as potential grid materials (Table 1) for high temperature applications. The choice criteria were their high melting temperature (in comparison with the creep test temperature range investigated in this study [700–850 °C]) and their electron backscattering factor (Heinrich's calculation of η_r was employed [10] associated to the pure element electron backscattering coefficient η obtained by Reuter [11]). For comparison, the backscattering factor computed for the superalloy NR6 used as substrate is evaluated to be 0.292.

The materials were deposited in the form of microgrids on NR6 samples which were heated in the creep machine furnace (without load) at 750 °C for durations between 72 and 460 h. These experiments were carried out under vacuum ($\sim 10^{-4}$ Pa) and with getter materials (TiZr shavings and Nb strips) close to the specimen in order to minimize oxidation. After exposure at 750 °C, Mo and W metallic grids exhibit significant degradation essentially due to oxidation issues. Molybdenum and tungsten silicides were subjected to a pest phenomenon described by several authors [12–14]. This catastrophic oxidation is supposed to occur at intermediate temperature (400–700 °C, during the slow heating before creep test). An illustration of this phenomenon is presented in Fig. 1. Figure 1b shows the significant damage of a WSi_2 grid after 460 h at 750 °C under vacuum as compared to the unexposed grid (Fig. 1a). These various types of grid degradation are certainly increased due to the thinness of the grid material deposit (10–30 nm). Unlike these materials, oxide grids presented

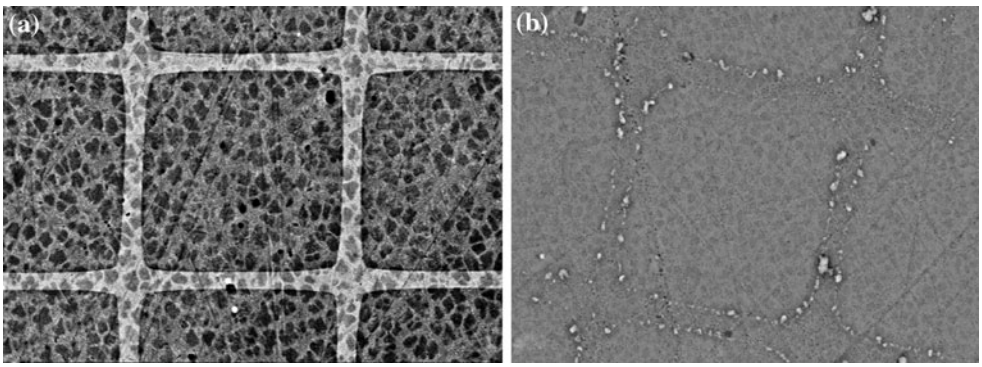

Fig. 1 WSi_2 grid (5 μm pitch): **a** before and **b** after exposure at 750 °C during 460 h (under vacuum ($\sim 10^{-4}$ Pa) and with getters close to the specimen) (SEM-BSE)

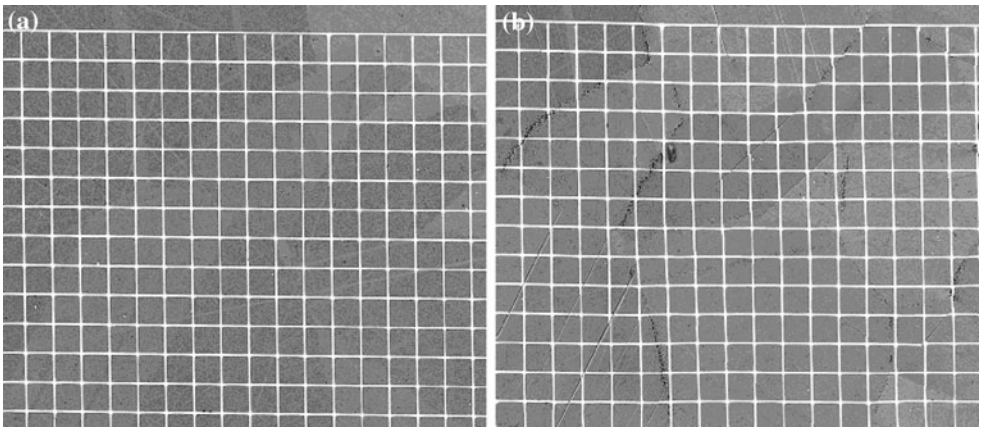

Fig. 2 HfO_2 grid (5 μm pitch): **a** before and **b** after creep test at 750 °C and 525 MPa during 150 h (under vacuum ($\sim 10^{-4}$ Pa) and with getters close to the specimen) (SEM-BSE)

high stability in the same conditions. HfO_2 was eventually selected on the base of higher BSE contrast (Fig. 2).

Microgrid deposition technique

Microgrids were deposited on the widest surface of a flat creep specimen using an electron lithography technique schematised in Fig. 3. Grids were obtained at the end of a five-step procedure:

1. The surface was prepared by mechanical polishing (1/4 μm diamond spray) followed by careful cleaning. Polymethyl methacrylate (PMMA) resins were used as electron-sensitive resists. A two-layer coat was deposited by successive centrifugations and bakings (1 h at 150 °C). The technique lies in superimposing PMMA resins of different molar masses. The top coat resin is a high molar mass PMMA (996,000 g mol^{-1}) and the bottom coat resin is a low one (350,000 g mol^{-1}). The shape of the two-layer coat obtained in this way promotes the final resist removal and ensures thicker grid deposit [15].
2. The two-layer PMMA resin was irradiated by electron beam. This step was carried out in a SEM with computer-monitored electron beam displacement. Irradiation conditions were defined to obtain grids with continuous and narrow lines and are presented in Table 2 for a 300 nm two-layer coat thickness. This set of conditions ensured the production of microgrids with a 5 μm pitch and a maximum width line of 0.5 μm. The grid dimensions were about 318 μm × 318 μm.
3. Because of the interactions with electrons, irradiated resin had shorter molecular chains than non-irradiated one. For this reason, the irradiated resin is more easily dissolved. The removal of this resin reveals substrate lines under the electron scanning pattern. The solvent used for this stage is made up of 70 vol% of isopropylic alcohol and 30 vol% of methyl ethyl ketone.
4. The grid material was then deposited by sputtering (Gatan Model 682 PECS™). The coat thickness (10–30 nm) was controlled by a piezoelectric sensor.

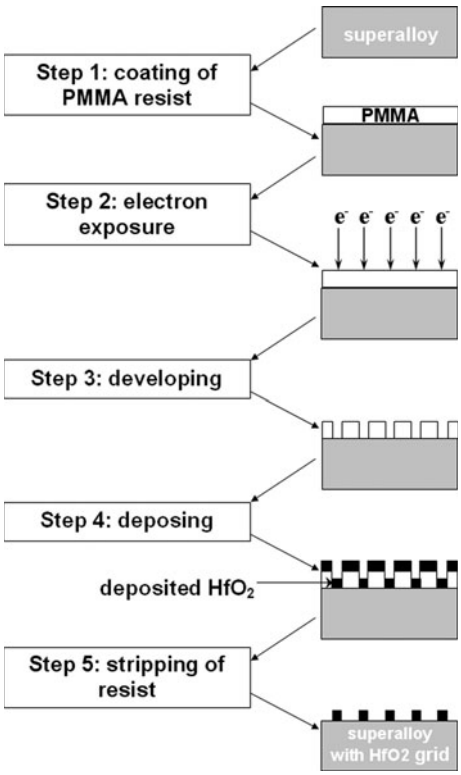

Fig. 3 Sequence of the microlithography technique

Table 2 Electron beam irradiation parameters (for a 300 nm two-layer coat thickness)

Accelerating voltage	Working distance	Probe current	Irradiation time for one line
25 kV	25 mm	0.07 nA	1 s

5. The removal of the resist used to mask the substrate from the coating material is provided by dissolution of the non-irradiated PMMA resin in chloroform.

Deformation analysis procedure

The microgrid size was chosen to cover a statistically representative area while avoiding grid defaults resulting from SEM deflection defocusing. Analysis of both intragranular deformation and GBS imposes that each grain contains several grid crosses, and each grain boundary is intercepted by several grid lines. Moreover, a sufficient number of grains must be covered by the overall grid to get good statistics. The mean grain size of the NR6 superalloy being about 25 μm, the choice of 318 μm × 318 μm grids therefore allows to include about 150 grains and about 600 grain boundaries (Fig. 4).

The micrographs in Fig. 5 show the various elementary phenomena observed during creep of the NR6 superalloy.

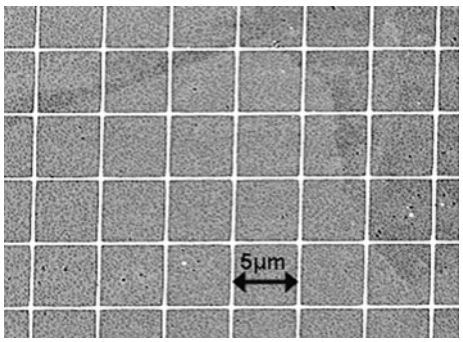

Fig. 4 Grain size in comparison with the cell size (SEM-BSE)

Intragranular slip bands (a), plasticity close to grain boundary (b), GBS (c), grain boundary cracking (d) as well as fold at triple point (e) are clearly evidenced by the deformation of the microgrid. An accurate displacement measurement method has been implemented to quantify these phenomena and their relative importance.

Nine high resolution (4096 pixels × 4096 pixels) SEM images were recorded for each grid and were combined to build up a single image of the grid. These operations were carried out before and after creep deformation. Standard image correlation is based on grey level distribution of different objects. This method could not be used here because creep tests led to some degradation of this distribution. High local deformation and slight superalloy oxidation could indeed induce these changes. So, a specific image analysis procedure was developed and applied during this work to quantify in-plane displacement fields.

A cross-like grid node pattern is selected for each image (Fig. 6b). A cross-correlation is carried out by sliding this pattern along the image (Fig. 6a) and by calculating the normalized correlation coefficient at each pixel (Fig. 6c). The position of a grid node is combined with the local maxima of the correlation function (or with the barycentre of a maxima set). The positions of the nodes for each state (before and after creep) are recorded in two files. To match the nodes of the two files, the grid is built back from the nodes (Fig. 7). The grid mesh is carried out by Delaunay triangulation [16] (Fig. 7b) and then by merging two adjacent triangles to form a quadrangle (Fig. 7c). The central node of the "before creep" grid is matched with the one of the "after creep" grid as they are arbitrary considered as reference nodes.

Analysis of local strain and GBS

Local strain calculation

Once the nodes are matched, in-plane displacement vector $\vec{U}$ at the node A of coordinates (x, y) can be calculated as follows:

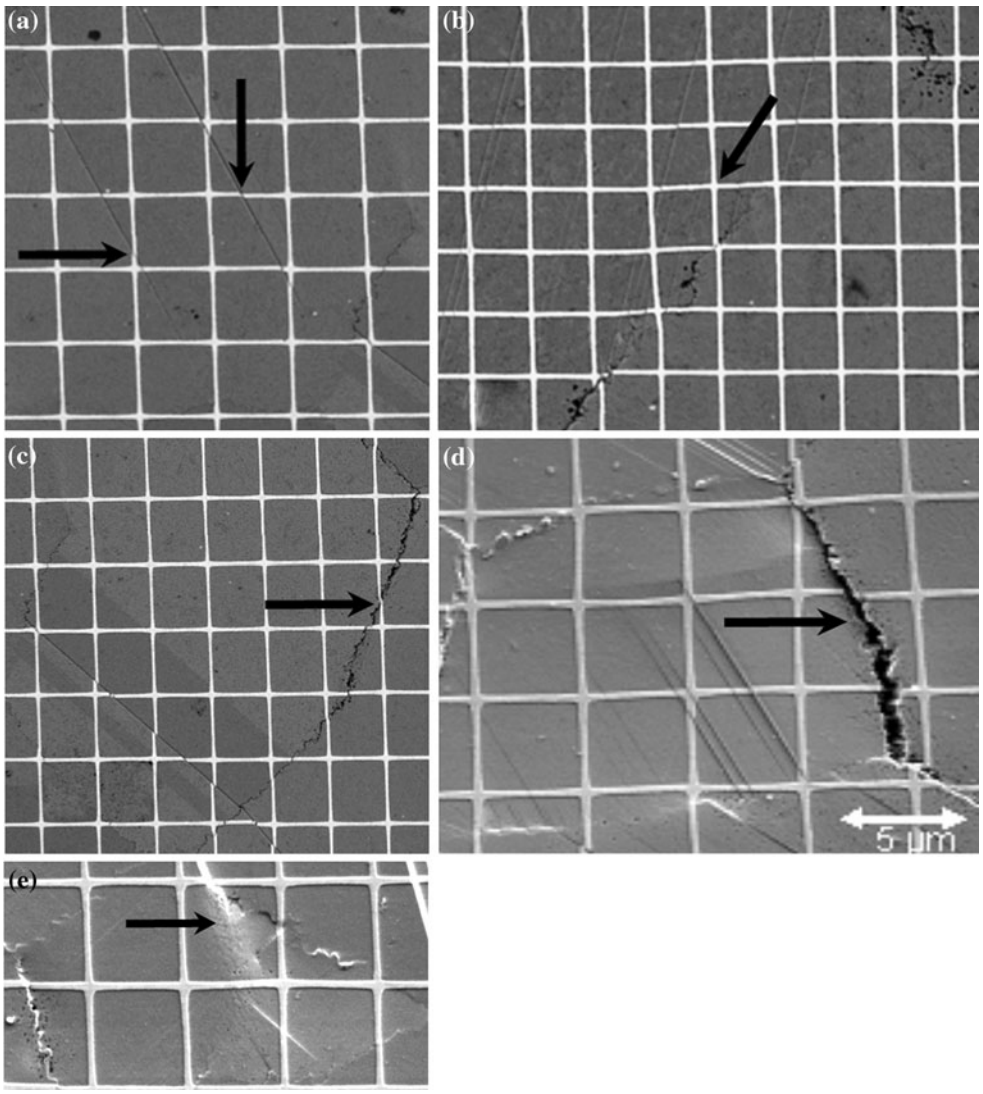

Fig. 5 HfO_2 grid (5 µm pitch) after creep at 750 °C and 525 MPa: **a** intragranular slip bands; **b** plasticity close to grain boundary; **c** GBS; **d** grain boundary cracking; **e** fold at triple point. **a**, **b**, **c** $\varepsilon = 1.7\%$ (SEM-BSE) and **d**, e $\varepsilon = 3.5\%$ (SEM-secondary electrons)

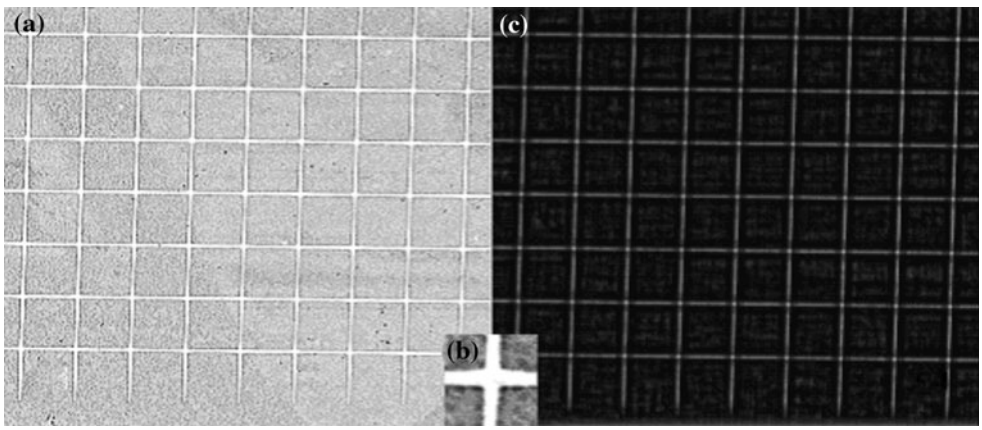

Fig. 6 Node correlation: **a** SEM grid image (BSE); **b** node pattern; **c** display of the correlation coefficient file

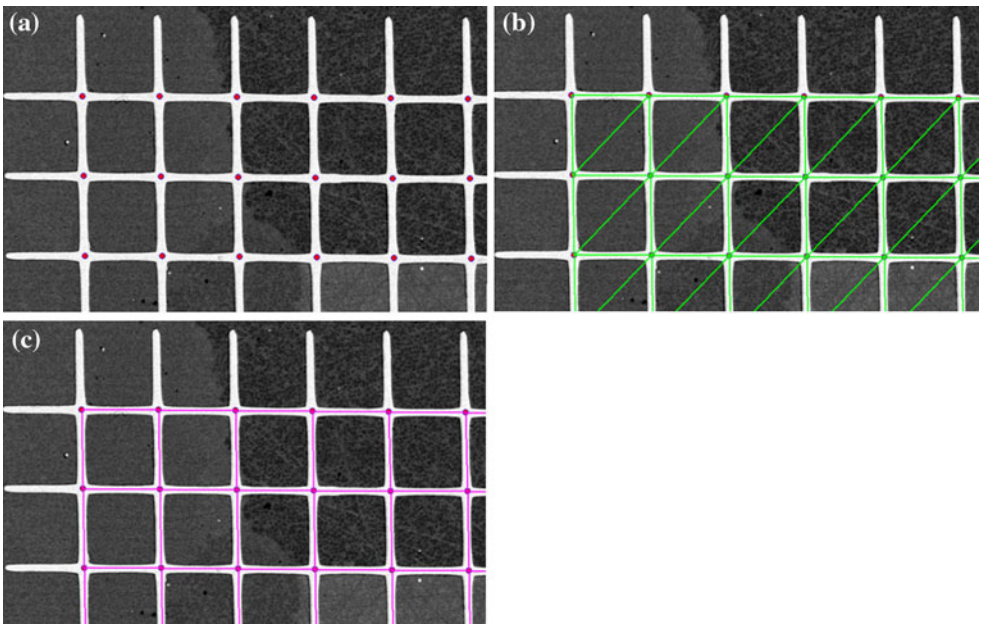

Fig. 7 Grid meshing (5 μm pitch): **a** grid node network; **b** triangle network; **c** quadrangle network

$$\vec{U}(x,y) = A(x,y) - A'(x,y) \tag{1}$$

where $A(x, y)$ is the initial position and $A'(x, y)$ is the final position of the node A of coordinates (x, y).

For the evaluation of the in-plane deformation, the Green–Lagrange tensor of deformation, E, is computed at each node. In small-deformation theory, the tensor, E, can be approximated by ε as follows:

$$\varepsilon = \frac{1}{2}\begin{pmatrix} 2\frac{\partial U_x(x,y)}{\partial x} & \frac{\partial U_x(x,y)}{\partial y} + \frac{\partial U_y(x,y)}{\partial x} \\ \frac{\partial U_x(x,y)}{\partial y} + \frac{\partial U_y(x,y)}{\partial x} & 2\frac{\partial U_y(x,y)}{\partial y} \end{pmatrix} \tag{2}$$

where $U_x(x, y)$ and $U_y(x, y)$ are the components of the displacement vector $\vec{U}$, respectively, along the x- and y-axes for the node of coordinates (x, y). The derivatives are then evaluated using the difference of the displacements between neighbouring grid points.

The discretization of the three deformation components at the node (x, y) leads to the following formulae:

$$\varepsilon_{xx}(x,y) \approx \frac{U_x((x-\Delta x),y) - U_x((x+\Delta x),y)}{|2\Delta x|} \tag{3}$$

$$\varepsilon_{yy}(x,y) \approx \frac{U_y(x,(y-\Delta y)) - U_y(x,(y+\Delta y))}{|2\Delta y|} \tag{4}$$

$$\varepsilon_{xy}(x,y) \approx \frac{1}{2}\left(\frac{U_x(x,(y-\Delta y)) - U_x(x,(y+\Delta y))}{|2\Delta y|} + \frac{U_y((x-\Delta x),y) - U_y((x+\Delta x),y)}{|2\Delta x|}\right) \tag{5}$$

The integration domain is defined by the four closely related nodes of the node under consideration. In the present case, the displacement is integrated with $\Delta x = \Delta y = 5$ μm which is the grid pitch (Fig. 8). An illustration of the local strain field is presented in Fig. 9. In Fig. 9a is presented a part of a grid and in Fig. 9b the associated strain field after a creep test at 750 °C and 535 MPa interrupted at a deformation of 1.7%.

Fig. 8 Integration field of the deformation tensor at the central node

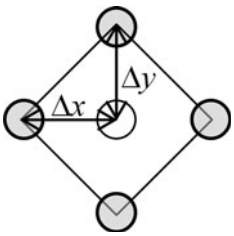

GBS calculation

Strain field calculations do not allow direct quantification of the GBS. The deformations calculated at nodes on both sides of a grain boundary underestimate the GBS, which, by nature, is localized in a very narrow zone, of the order of the grain boundary thickness. To obtain a more realistic calculation of the GBS, a specific method was developed.

Grain boundary sliding (GBS) between two grains leads to the occurrence of offsets along the lines of the grid (Fig. 10). In-plane GBS deformation was defined by the sliding vector as follows:

Each node of the grid is characterized by its coordinates (x, y) and its displacement vector $\vec{U}$ (Eq. 1). Let A and B be the nodes on both sides of a grain boundary (Fig. 11a). After creep test, the nodes A and B change in A' and B'

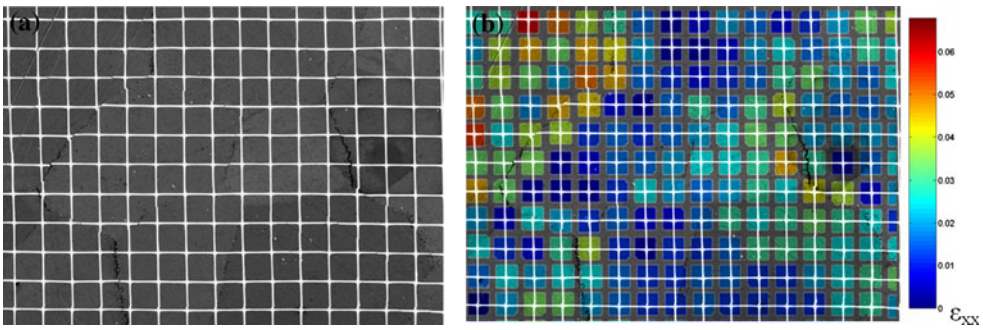

Fig. 9 Specimen crept at 750 °C and 535 MPa, $\varepsilon = 1.7\%$ (horizontal tensile axis) (5 μm pitch): **a** SEM image (secondary electrons); **b** associated deformation map (ε_{xx})

(Fig. 11b). As illustrated in Fig. 11c, the in-plane GBS vector $\vec{S}$ is defined by:

$$\vec{S} = \vec{U}_B - \vec{U}_A \tag{6}$$

A grain boundary intercepts several lines of the grid so it is characterized by several GBS vectors $\vec{S}$. At a given grain boundary, the GBS is quantified by:

– local sliding values S_i, local GBS amplitude at the intercept i:

$$S_i = \sqrt{S_x^2 + S_y^2} \tag{7}$$

where S_x and S_y are the components of $\vec{S}$ parallel and perpendicular to the tensile axis, respectively

– a mean GBS defined by:

$$S_{\text{mean}} = \frac{1}{N}\sum_{i=1}^{N} S_i \tag{8}$$

where N is the number of intercepts for a given grain boundary.

According to [17], the contribution, ξ, of the GBS to the overall deformation (along the tensile axis) can be written as

$$\xi = \frac{\varepsilon_{\text{GBS}}^{//}}{\varepsilon_{\text{t}}} \tag{9}$$

There, ε_{t} represents the mean plastic deformation along the tensile axis measured from the average of all the ε_{xx} calculated at each node of the grid ($\varepsilon_{\text{t}} = \bar{\varepsilon}_{xx}$) and $\varepsilon_{\text{GBS}}^{//}$ the mean GBS value projected along the tensile axis. $\varepsilon_{\text{GBS}}^{//}$ is defined as follows [18]:

$$\varepsilon_{\text{GBS}}^{//} = \frac{\bar{S}_x}{D_{\text{mean}}} \tag{10}$$

where $\bar{S}_x$ is the mean value of the components parallel to the tensile axis and D_{mean} is the mean grain size of the superalloy.

Measurement accuracy

The lines of the grid have to be defined by several pixels to determine accurately the grid node position. A magnification of 500 was chosen and a line width includes about 12 pixels. Similarly, the initial distance between two nodes (the grid pitch) counts about 120 pixels. At this magnification, the complete grid has to be composed of several (9) high resolution images (4096 pixels × 4096 pixels). The assembly of these images to build a single image of the grid (about 7800 pixels × 7800 pixels) is a delicate task and can induce some local inaccuracy if not carefully controlled.

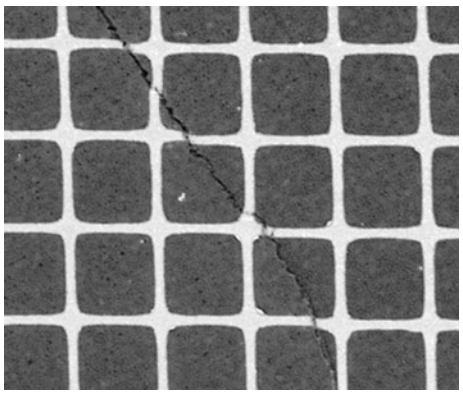

Fig. 10 GBS events observed after creep test at 850 °C and 350 MP, $\varepsilon = 1\%$ (SEM-BSE) (5 μm pitch) (horizontal tensile axis)

The main sources of inaccuracies in the final values are due to the image acquisition in the SEM, to the image correlation technique and also to the image processing used to calculate the local strain or GBS values. The inaccuracies due to the image acquisition and to the image correlation technique were evaluated by recording successively two high resolution images (4096 pixels × 4096 pixels) of the same area or by recording high resolution images before and after specimen repositioning. The correlation technique applied to these images allows determining the global deformation due to the imaging process (the duration for recording a high resolution image is about 40 min during which a drift of the electron beam is expected). The correlation technique itself was estimated to detect the grid node position with an accuracy of one pixel. Analysis of these experiments shows globally that the measurement error was evaluated to be in the order of two pixels for displacement field and of 0.3% for strain field.

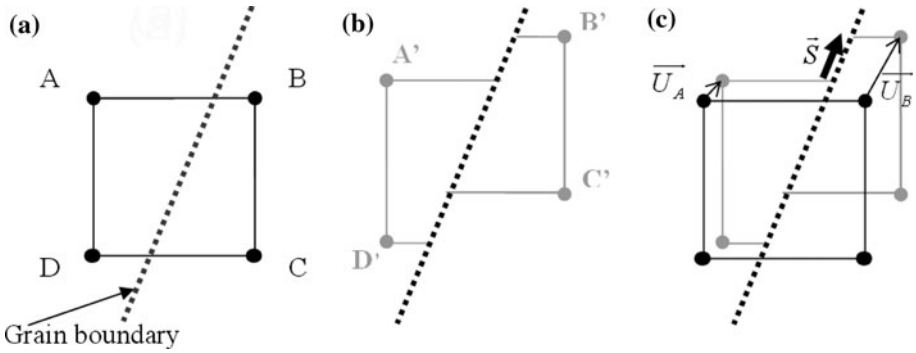

Fig. 11 Calculation method for the displacement vector $\vec{S}$: **a** node positions in the initial cell; **b** node positions after GBS event; **c** specification of the in-plane GBS vector $\vec{S}$

Combined information of grain boundary crystallography and GBS

All the data obtained at each grid/grain boundary intercept have to be gathered together in a single file to statistically analyse the grain boundary deformation according to various grain boundary parameters.

EBSD analysis was performed on grid areas of each creep specimen before creep test in a Zeiss DSM 960 SEM equipped with the OIM^{TM} software from TSL. In this study, the grain boundaries were defined as boundaries with a misorientation angle greater than 10°. Grain boundaries were classified using the coincidence site lattice (CSL) model and Brandon's criterion given by:

$$\Delta\theta_{\max} = 15^{\circ}\Sigma^{-1/2} \tag{11}$$

where Σ is the character of the grain boundary according to the CSL model and $\Delta\theta_{\max}$ is the maximum allowable deviation to this exact coincidence.

The set of grain boundaries were thus categorized in two classes: the CSL boundaries defined by $3 \leq \Sigma \leq 29$ and the general (or random) boundaries defined by no coincidence or $\Sigma > 29$. The CSL boundary class was dissociated in two subclasses; $\Sigma 3$ were considered as twin boundaries and the other boundaries ($3 < \Sigma \leq 29$) as CSL boundaries. Average proportions of the defined classes are given in Table 3. A specific software was developed at ONERA to build a continuous grain boundary network from the EBSD map. This program also provided in a single file grain boundary geometrical parameters (length, angle to the tensile axis,…) in addition to the grain boundary character.

In order to merge the grain boundary data obtained from the EBSD map and the ONERA software with the GBS data resulting from calculations on grid images, it was then necessary to superimpose the EBSD map on the grid image. These two data sets (EBSD map and grid image) were acquired in two different SEM at different magnifications and at different specimen tilts. EBSD maps were indeed obtained with the sample tilted at 70° for optimum diffraction acquisition while grid images were recorded at 0° tilt. In order to precisely superimpose the EBSD map on grid image, a specific algorithm based on homography principle was developed. Using this function, the overlay of EBSD map on local strain map or GBS amplitude map is made possible. An example is shown in Fig. 12 where the GBS amplitude map is superimposed on the EBSD map for a specimen crept at 700 °C and 700 MPa (1% plastic strain).

Table 3 Grain boundary character distribution in NR6 superalloy

GB class	Number fraction (%)
$\Sigma 3$	37
$3 < \Sigma \leq 29$	9
$\Sigma > 29$	54

Application to NR6 superalloy

Material

The development of future aero engines requires the turbine inlet temperature increase or/and the improvement of engine durability. These extreme conditions will promote creep phenomena in the hottest areas of the turbine disc. Accurate analysis of creep deformation mechanisms of disc superalloys, when long durations and high temperatures are combined, therefore requires the use of a superalloy suited for these harsh conditions. The material selected for this study is the NR6 nickel-base disc superalloy developed at ONERA to exhibit an excellent thermal stability (no deleterious σ or μ phases after 10,000 h at 700 °C) and a high creep resistance [19]. NR6 is a powder metallurgy (PM) superalloy processed as follows: vacuum induction melting, argon atomization, sieving (<75 μm (−200 mesh)), hot compaction, hot extrusion and isothermal forging. Its chemical composition is presented in Table 4.

The austenitic nickel-rich γ matrix is strengthened by a volume fraction of about 45% of ordered $L1_2$ γ'-Ni_3Al precipitates. A coarse-grained microstructure was chosen to promote high temperature creep strength. The following

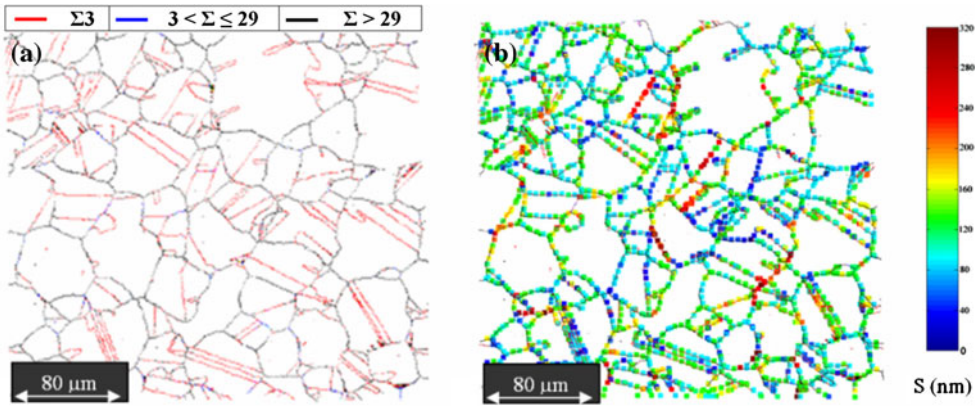

Fig. 12 Maps of a specimen crept at 700 °C and 700 MPa, $\varepsilon = 1\%$ (horizontal tensile axis): **a** EBSD map; **b** Superimposing of GBS amplitude (S) map on the EBSD map

Table 4 NR6 chemical composition (wt%)

Ni	Co	Cr	Mo	W	Al	Ti	Hf	B	C	Zr
Bal.	14.8	14.0	2.0	4.1	3.1	4.5	0.33	0.012	0.023	0.053

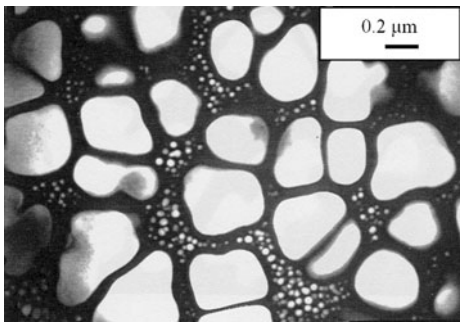

Fig. 13 Secondary and tertiary γ' precipitates in NR6 superalloy (TEM dark field image)

heat treatment sequence was applied on all the creep specimens: 1190 °C for 2 h (~100 °C/min cooling) + 700 °C for 24 h (air cooling) + 800 °C for 4 h (air cooling). The γ' solvus temperature of NR6 alloy is around 1175 °C, the mean grain size measured after this supersolvus solution treatment is about 26 µm. At the end of the heat treatment sequence, the grains contain two γ' precipitate populations (Fig. 13). The mean secondary (cooling) γ' precipitate size is about 225 nm and the tertiary (ageing) γ' precipitate size is in the 10–40 nm range.

Creep conditions

Constant load tensile creep tests were conducted on flat specimens. The microgrids were deposited at the centre of the large face of the specimens (gauge: 31 mm length, 4.2 mm width and 2.5 mm thickness) (Fig. 14). In order to minimize oxidation of the superalloy and the degradation of the microgrids, all the creep tests were performed under vacuum (~10^{-4} Pa) and with getter materials close to the specimen. Creep tests were carried out in the 700–850 °C and 350–700 MPa ranges. Minimal creep rates were in the 2.10^{-6} to 5.10^{-9} s^{-1} range.

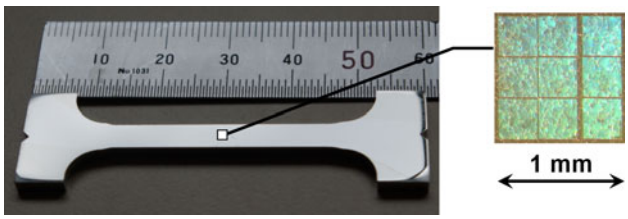

Fig. 14 Location of the microgrids on the flat creep test specimen

Quantitative evaluations of the local strains and of GBS were done at 1% plastic strain for all the specimens except one for which these data were computed between 1.7 and 5% plastic strain (the failure of the specimen occurred at 5.5%). These experimental conditions allowed studying the effect of temperature, applied stress and global strain level on the local strains and on the GBS.

Examples of results obtainable by the grid method

Influence of the creep temperature on the local strain and on the GBS

Creep tests were conducted at high stress (700 MPa) and at 700 and 800 °C to study the influence of the temperature on the local strain and on the GBS amplitude. Local strain maps and GBS amplitude maps are presented in Fig. 15. These results indicate that the higher the temperature, the more homogeneous the deformation within the grains and between neighbouring grains. They also show that the higher the temperature, the lower the GBS value, and the lower its relative contribution to the overall strain. This is confirmed by the calculated values of S_{mean} and the GBS contribution ξ tabulated in Table 5. Indeed shearing of the fine γ' precipitates by matrix dislocations in the superalloy grains promotes localization of the deformation within narrow and planar slip bands [20, 21]. This heterogeneous deformation mechanism induces stress concentrations at

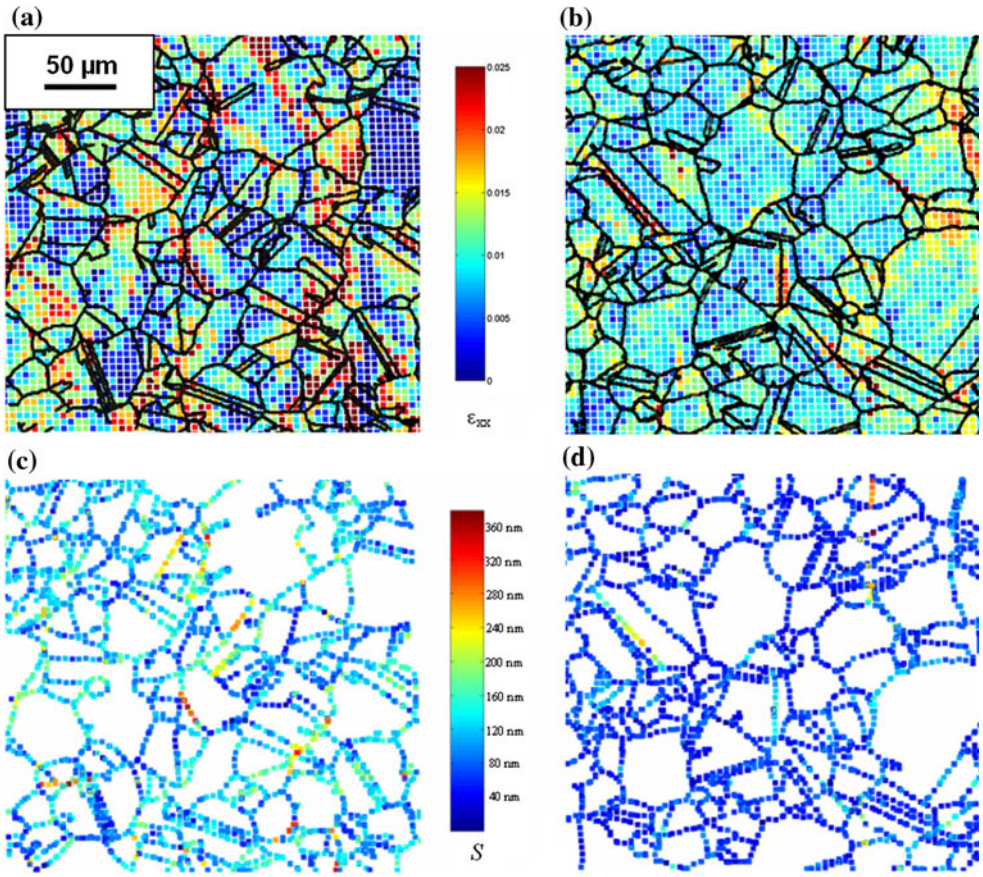

Fig. 15 Local strain ε_{xx} (**a**) and (**b**) and GBS amplitude S (**c**) and (**d**) maps after creep test at 700 MPa and 700 °C (**a** and **c**) or 800 °C (**b** and **d**) (horizontal tensile axis)

Table 5 S_{mean} and ξ values for creep tests at 700 MPa

Creep temperature (°C)	Mean GBS S_{mean} (nm)	GBS contribution ξ
700	113	0.33
800	60	0.19

the intersections between the slip bands and the grain boundaries which promote GBS. The higher the temperature, the more homogeneous the deformation because it becomes easier for matrix dislocations to circumvent the precipitates through thermally activated mechanisms such as climb and cross-slip, and the lower the GBS amplitude.

Influence of grain boundary character on GBS

Using the tools developed in this work, the influence of the GB character on the GBS was analysed in function of the creep conditions. S_{mean} values of the different GB classes are presented in Fig. 16 for two creep temperatures (800 and 850 °C) at the same creep stress of 350 MPa. At 350 MPa and 800 °C, the GBS amplitude S_{mean} is highest for the random GB and lowest for the twin boundaries. This structural effect is explained by the greater ability of lattice dislocations to be absorbed and to dissociate into high angle grain boundaries (random GB) [22–24]. However, as

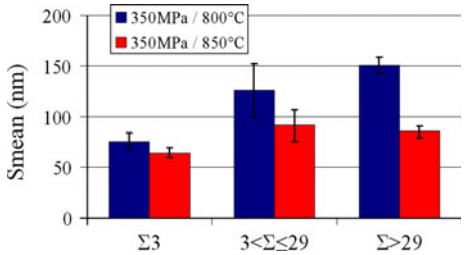

Fig. 16 Influence of the GB character and creep temperature on the S_{mean} at 350 MPa

the temperature increases, the influence of the grain boundary character on the GBS decreases. At 850 °C, the difference between the S_{mean} values of the random GB and the CSL GB is reduced. This tendency was already observed in other studies [25–27] and was correlated with an increase of the influence of the grain boundary diffusion at high temperature.

Conclusion

A microgrid extensometry technique especially suitable for analysis of high temperature creep behaviour of metallic materials was developed to obtain, in a quantitative and

statistically representative manner, information on intragranular deformation (including strain distribution) and on GBS. Coupled with EBSD technique, it was demonstrated to be an efficient tool to analyse the deformation mechanisms operating during creep of a nickel-base disc superalloy. More specifically, it has been possible to quantify, by direct measurements, the effect of GB crystallographic nature and geometrical orientation with respect to the tensile axis, on its ability to undergo GBS. Detailed results of a more comprehensive study on the creep behaviour of this alloy using this new experimental method will be published in a forthcoming paper.

References

1. Frost HJ, Ashby MF (1982) Deformation-mechanism maps. Pergamon Press, Oxford, UK
2. Denison JP, Holmes PD, Wilshire B (1978) Mater Sci Eng 33:35
3. Parker JD, Wilshire B (1977) Mater Sci Eng 29:219
4. Karimi A (1984) Mater Sci Eng 63:267
5. Carolan RA, Egashira M, Kishimoto S, Shinya N (1991) Mater T JIM 32(1):67
6. Héripré E, Dexet M, Crépin J, Gélébart L, Roos A, Bornert M, Caldemaison D (2007) Int J Plasticity 23:1512
7. Pinna C, Beynon JH, Sellars CM, Bornert M (2000) In: Martin P et al (eds) Proceedings of conference on mathematical modelling in metal processing and manufacturing (COM 2000) (only CD)
8. Soula A, Renollet Y, Boivin D, Pouchou J-L, Locq D, Caron P, Bréchet Y (2008) In: Reed RC et al (eds) Proceedings of superalloys 2008, p 387
9. Soula A, Renollet Y, Boivin D, Pouchou J-L, Locq D, Caron P, Bréchet Y (2009) Mater Sci Eng A 510–511:301
10. Heinrich KFJ (1966) In: Castaing R et al (eds) Proceedings of the 4th international conference on X-ray optics and microanalysis X, p 159
11. Reuter W (1972) In: Shinoda G et al (eds) Proceedings of the 6th international conf. on X-ray optics and microanalysis X, p 121
12. Berztiss DA, Cerchiara RR, Gulbransen EA, Pettit FS, Meier GH (1992) Mater Sci Eng A 155:165
13. Yanagihara K, Maruyama T, Nagata K (1996) Intermetallics 4(1):133
14. Liu YQ, Shao G, Tsakiropoulos P (2001) Intermetallics 9:125
15. Charlebois S (2002) PhD thesis, Sherbrooke, Canada
16. George PL, Borouchaki H (1998) Triangulation and meshing application to finite elements. Hermes, Paris
17. Langdon TG (2006) J Mater Sci 41:597. doi:10.1007/s10853-006-6476-0
18. Bell RL, Graeme-Barber C, Langdon TG (1967) T Metall Soc AIME 239(11):1821
19. Locq D, Marty M, Walder A, Caron P (2000) In: Morris DG et al (eds) Proceedings of euromat 99 intermetallics and superalloys, vol 10, p 52
20. Viswanathan GB, Sarosi P, Henry M, Whitis D, Mills M (2004) In: Green KA et al (eds) Proceedings of superalloys 2004, p 173
21. Locq D, Caron P, Raujol S, Pettinari-Sturmel F, Coujou A, Clément N (2004) In: Green KA et al (eds) Proceedings of superalloys 2004, p 179
22. Kokawa H, Watanabe T, Karashima S (1983) J Mater Sci 18:1183. doi:10.1007/BF00551988
23. Kokawa H, Watanabe T, Karashima S (1981) Philos Mag A44(6):1239
24. Pond RC, Smith DA, Southerden PWJ (1978) Philos Mag A37(1):27
25. Kergaravat J-F (1996) PhD Thesis, Grenoble France
26. Weinberg F (1958) T Metall Soc AIME 212:808
27. Priester L (1989) Rev Phys Appl 24:419